EDGE ARTICLE

Check for updates

Selective adsorption of fluorinated super greenhouse gases within a metal–organic framework with dynamic corrugated ultramicropores†

Bevan S. Whitehead, [ID] [a] William W. Brennessel, [ID] [a] Shane S. Michtavy, [ID] [b] Hope A. Silva, [a] Jaehwan Kim, [ID] [c] Phillip J. Milner, [ID] [c] Marc D. Porosoff [ID] [b] and Brandon R. Barnett [ID] *[a]

Perfluorocompound (PFC) gases play vital roles in microelectronics processing. Requirements for ultra-high purities traditionally necessitate use of virgin sources and thereby hinder the capture, purification, and reuse of these costly gases. Most importantly, gaseous PFCs are incredibly potent greenhouse gases with atmospheric lifetimes on the order of 10^3–10^4 years, and thus any environmental emissions have an outsized and prolonged impact on our climate. The development of sorbents that can capture PFC gases from industrial waste streams has lagged substantially behind the progress made over the last decade in capturing CO_2 from both point emission sources and directly from air. Herein, we show that the metal–organic framework Zn(fba) (fba^{2-} = 4,4'-(hexafluoroisopropylidene)bis-benzoate) displays an equilibrium selectivity for CF_4 adsorption over N_2 that surpasses those of all water-stable sorbents that have been reported for this separation. Selective adsorption of both CHF_3 and CH_4 over N_2 is also evident, demonstrating a general preference for tetrahedral C_1 gases. This selectivity is enabled by adsorption within narrow corrugated channels lined with ligand-based aryl rings, a site within this material that has not previously been realized as being accessible to guests. Analyses of adsorption kinetics and X-ray diffraction data are used to characterize sorption and diffusion of small adsorbates within these channels and strongly implicate rotation of the linker aryl rings as a gate that modulates transport of the C_1 gases through a crystallite. Multi-component breakthrough measurements demonstrate that Zn(fba) is able to resolve mixtures of CF_4 and N_2 under flow-through conditions. Taken together, this work illuminates the dynamic structure of Zn(fba), and also points toward general design principles that can enable large CF_4 selectivities in sorbents with more favorable kinetic profiles.

aDepartment of Chemistry, University of Rochester, Rochester, NY, USA. E-mail: brandon.barnett@rochester.edu

bDepartment of Chemical Engineering, University of Rochester, Rochester, NY, USA

cDepartment of Chemistry and Chemical Biology, Cornell University, Ithaca, NY, USA
† Electronic supplementary information (ESI) available. CCDC 2321191–2321195. For ESI and crystallographic data in CIF or other electronic format see DOI: https://doi.org/10.1039/d3sc07007g

Introduction

The capture of anthropogenically emitted greenhouse gases (GHGs) is a central endeavor toward mitigating the worst impacts of climate change.[1–3] Carbon dioxide capture, both from point emission sources and directly from air, merits outsized attention given the sheer quantities of CO_2 that are emitted relative to other GHGs.[4–8] However, capping warming at 1.5 °C over pre-industrial levels will likely require mitigation of other GHGs which, although emitted in smaller quantities, possess greater heat-trapping potentials. For instance, methane

is emitted in substantially smaller quantities than CO_2, yet is responsible for more than 10% of GHG-related warming on account of its large Global Warming Potential (GWP).[9]

Amongst the most potent GHGs are gaseous per-fluorocompounds (PFCs) and hydrofluorocarbons (HFCs). Owing to their intense heat-trapping capabilities and kinetic inertness to atmospheric conditions, gases such as tetra-fluoromethane (CF_4), trifluoromethane (CHF_3), hexafluoro-ethane (C_2F_6), nitrogen trifluoride (NF_3), and sulfur hexafluoride (SF_6) possess GWPs that are orders of magnitude higher than that of CO_2 (Fig. 1).[10,11] These fluorinated gases play vital roles in the microelectronics industry and see widespread usage in semiconductor manufacturing, where they are used as plasma etchants and cleaning agents for deposition chambers.[10,12] Importantly, the low utilization efficiency for CF_4 in particular during plasma etching can result in substantial environmental emissions from etch gas exhaust. Existing abatement methods focus on destruction of remnant PFC gas in
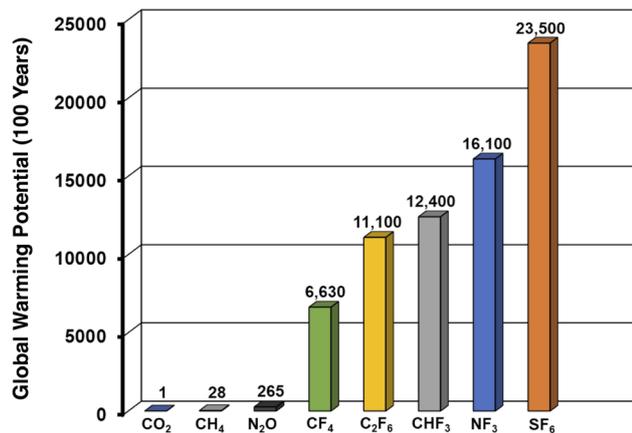
Fig. 1 One hundred year global warming potentials (GWPs) of various fluorinated and non-fluorinated greenhouse gases.

exhaust streams, and also yield problematic and caustic byproducts (e.g. HF, NO_x).[13–15] Tetrafluoromethane emissions also result from so-called "anode effects" during aluminum smelting.[16] Capture processes that facilitate the recovery and recycling/reuse of PFC gases remain, to our knowledge, unimplemented on industrial scales, a consequence of the dearth of selective and non-destructive separation methods and the very high purities required for industrially utilized PFCs.

Porous crystalline adsorbents (e.g. metal–organic frameworks; covalent–organic frameworks; zeolites) represent versatile and tunable classes of materials that offer promise in myriad gas capture and separation processes.[4,17–22] The design of sorbents exhibiting equilibrium selectivity toward a particular adsorbate requires a knowledge of potential modes of physical and/or chemical adsorption. For instance, the acidic nature of CO_2 facilitates chemisorption within adsorbents bearing basic functional groups (e.g. amines), allowing appropriately functionalized sorbents to achieve very high selectivities for CO_2.[4] In contrast, chemical handles to facilitate strong adsorption of either methane or tetrafluoromethane are limited owing to their kinetically inert natures, their lack of dipole or quadrupole moments, and their low polarizabilities.[23] Unlike some other fluorocarbons, the C–F bonds in CF_4 do not possess pronounced σ-holes that could facilitate strong halogen bonding interactions.[24,25] Porous materials that exhibit selectivity for nonpolar CF_4 over inert carrier gases such as N_2 have often employed ultramicropores (pore diameter <7 Å) so as to maximize van der Waals contacts with CF_4 and achieve strong physisorption.[26–30]

Importantly, metal–organic frameworks (MOFs) present plentiful opportunities to modulate the dimensions and electronic character of their pores. Notwithstanding, studies reporting even single-component adsorption isotherms of CF_4 within MOFs are surprisingly few.[31–37] However, several of those that have been analysed rank among the most selective materials that have been reported for CF_4 capture from N_2 (Table S1†). For instance, Ni(ina)$_2$ (ina$^-$ = isonicotinate) and Ni(3-ain)$_2$ (3-ain$^-$ = 3-aminoisonicotinate) display the largest selectivities

reported for this mixture (46.3 and 34.7, respectively, for 10 : 90 CF_4 : N_2 at 298 K and 1 bar).[33] Other MOFs displaying high thermodynamic selectivities include Ni(O_2CH)$_2$ and Ni(adc)(dabco)$_{0.5}$ (25 and 23, respectively, for 10 : 90 CF_4 : N_2 at 298 K and 1 bar).[34,35] All of these materials share the structural trait of bearing ultramicropores; however, we note that CF_4 adsorption kinetics were not investigated for any of the above materials. Although rapid kinetic profiles are essential for adsorptive separations that exploit equilibrium selectivities, kinetic studies are frequently omitted from literature reports. Kinetics investigations in ultramicroporous materials are particularly pertinent, given that even small-profile adsorbates such as CF_4 (kinetic diameter of 4.7 Å)[23] are likely to be of a similar size to that of the pores.

The ideal adsorbent for a real-world PFC capture application would exhibit not only high capacity and selectivity, and a favorable kinetic profile, but also hydrophobicity to allow for capture from humid gas streams. Bent and fluorinated dicarboxylate linkers comprise a variety of metal–organic frameworks that bear ultramicroporous and hydrophobic character.[38–41] One such material is Zn(fba) (fba^{2-} = 4,4'-(hexafluoroisopropylidene)bis-benzoate), which was first reported by Monge in 2005.[42] Synthesized solvothermally in neat water, Zn(fba) contains one-dimensional cylindrical channels (6.0 Å diameter) that are lined with –CF_3 groups from the linker backbone. Additionally present are narrow corrugated channels, defined by the edges and faces of the aryl rings of the fba^{2-} linker, which had not previously been characterized as accessible sites for gas sorption. We demonstrate herein that the small spherical voids housed within these corrugated channels serve as the primary adsorption sites for CF_4. Importantly, these sites are ideally sized to accommodate CF_4, resulting in both strong physisorption ($\Delta H_{ads} = -32$ kJ mol^{-1}) and a large equilibrium selectivity over N_2. Similarly selective adsorption is seen for the hydrofluorocarbon gas CHF_3 and for CH_4, demonstrating that this material displays a general ability to strongly adsorb tetrahedral C_1 gases. The channel structure of Zn(fba) requires diffusion through narrow windows that are defined by the edges of four arene rings, which slows the diffusion of CF_4 through the pore network of a given crystallite. Using variable temperature transient adsorption measurements, we have determined the temperature dependence of the intracrystalline CF_4 diffusivity, which reflects local dynamics of the arene rings that modulate the effective window diameters. Despite this kinetic profile, multi-component breakthrough measurements confirm that separation of CF_4/N_2 mixtures is feasible at sufficiently slow flow rates.

Results and discussion

The solid-state structure of Zn(fba) is comprised of an infinite zinc-oxide rod building unit, wherein carboxylates bridge helical arrays of tetrahedrally coordinated Zn^{2+} centers traversing the crystallographic c axis (Fig. 2a). In addition to the fluoro-lined cylindrical channels, analysis of the activated structure using the Platon program CAVITY reveals that the arene-lined channels adopt a corrugated structure whereby
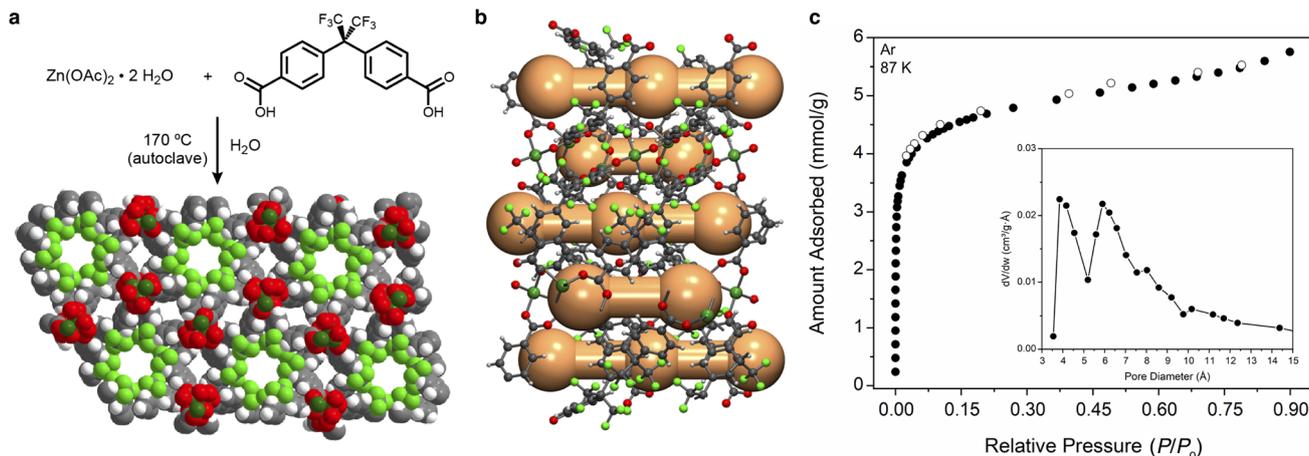
Fig. 2 (a) Synthesis and solid-state structure of Zn(fba) showing a cross-section of the two types of one-dimensional channels. A space-filling model is used wherein the van der Waals radii of atoms are depicted. Grey, white, red, light green, and dark green spheres correspond to carbon, hydrogen, oxygen, fluorine, and zinc atoms, respectively. (b) Cavity plot depicting the dimensions of the arene-lined channels in Zn(fba). These channels consist of spherical voids separated by narrow cylindrical windows. (c) Argon isotherm of Zn(fba) at 87 K. Filled and open circles correspond to adsorption and desorption points, respectively. (Inset) Pore size distribution plot derived from Ar isotherm data using a H−K model assuming spherical pores.

spherical voids (5.0 Å diameter) are connected through narrow cylindrical windows (3.0 Å diameter; Fig. 2b).

The corrugated profile is a reflection of the dihedral angle (65.3(9)°) between the geminal aryl rings in a given fba^{2-} linker, which forces ring edges to protrude into the channel and define the most constricted regions. To our knowledge, previous studies of gas adsorption and pore volume analysis of Zn(fba) have not characterized the arene-lined channels as potential adsorption sites.[42–44] The low-temperature isotherm data used to determine pore-size distributions (PSDs) in these works either incorporated minimal data points at very low relative pressures, or utilized N_2 as the probe molecule at 77 K – conditions which can prove insufficient to adequately characterize adsorption within constricted ultramicropores.[45] Accordingly, we utilized Ar as a probe at 87 K (Fig. 2c), while also employing a very long equilibration interval (180 s) to facilitate slow adsorbate diffusion. Analysis of this data using a Horvath–Kawazoe (H–K) kernel that assumes spherical pores yields a PSD that intimates accessibility of the corrugated arene-lined channels to the Ar probe.[46] As shown in Fig. 2c (inset), the resulting PSD plot contains distinct maxima at 4 Å and 6 Å, with the latter being consistent with the diameter of the trifluoromethyl-decorated cylindrical channels. The modest discrepancy in diameter sizes for the arene lined channels between the PSD plot and that found from structural analysis can be attributed to the limitations inherent to determining the textural properties of ultramicroporous materials.[45,47] Argon adsorption data was also used to calculate a BET surface area of 345(1) $m^2\ g^{-1}$ (Fig. S1†), which is in reasonable agreement with that reported by Yang et al. using Ar isotherm data.[44]

With an understanding of the pore structure of Zn(fba) in hand, adsorption isotherm measurements of tetrafluoromethane, trifluoromethane, and methane were carried out. At 298 K, all three adsorbates give rise to type I isotherm profiles (Fig. 3a). Uptake of CF_4 is notably steeper at low pressures

compared to CH_4, indicative of the former being adsorbed more strongly, with CF_4 also achieving substantially higher uptakes at the largest measured pressure (1200 mbar). As both adsorbates are non-polar, this difference is largely reflective of the optimal size match between tetrafluoromethane and the spherical voids, which maximizes van der Waals contacts. Owing to its electronic dipole moment, CHF_3 is adsorbed more strongly than CF_4 and displays larger uptake values at all measured pressures. This relative ordering is consistent with previous observations that non-polar CF_4 generally displays weaker adsorption strengths compared with polar C_1 HFC gases (e.g. CHF_3, CH_2F_2).[37] In contrast, uptake of N_2 at 298 K is minimal (Fig. 3a), as are uptakes of both O_2 and Ar (Fig. S2 and S3†).

Variable temperature isotherm measurements were used to determine differential enthalpies of adsorption (Fig. S4–S6 and Tables S2–S4†). Notably, the low-coverage value seen for CF_4 (−32.4(1) $kJ\ mol^{-1}$; Fig. 3b) is amongst the largest magnitude that has been reported in any sorbent material, and gives rise to a respectable capacity (1.05 $mmol\ g^{-1}$ at 298 K and 1 bar) despite the low surface area inherent to Zn(fba). Coupled with a minimal affinity for N_2, the result is a large equilibrium selectivity for CF_4 over N_2. At 10% CF_4, Ideal Adsorbed Solution Theory (IAST)[48] predicts a selectivity of 29 at 298 K and 1 bar (Fig. S7†). This selectivity value corresponds to a removal of 76% of CF_4 from the corresponding waste stream. Variable temperature CHF_3 isotherm data were used to determine a low-coverage differential adsorption enthalpy of −33.2(3) $kJ\ mol^{-1}$. For a 10% CHF_3 mixture in N_2, IAST predicts a selectivity of 75, which would correlate to a removal of 89% of gas-phase CHF_3 (Fig. S7†). While we suggest that Zn(fba) may be an excellent candidate for CHF_3 capture applications, a dearth of literature reporting adsorptive selectivities for CHF_3/N_2 mixtures obviates the comparison of this value to other sorbent materials.

Owing to the attention that's been given to decreasing industrial CF_4 emissions, along with the greater depth of
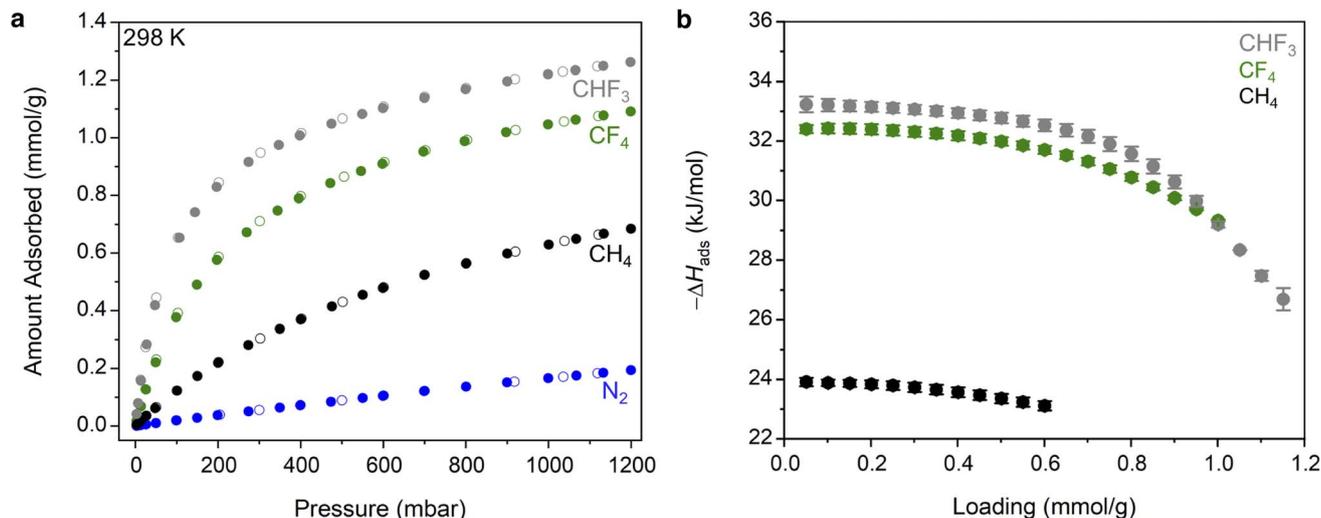
Fig. 3 (a) Adsorption isotherm data for CHF_3, CF_4, CH_4, and N_2 in Zn(fba) at 298 K. Filled and open symbols correspond to adsorption and desorption points, respectively. (b) Differential enthalpy of adsorption as a function of loading for CHF_3, CF_4, and CH_4. Error bars are shown for all data points.

literature investigating CF_4 sorption in porous materials, we chose to focus the remainder of our study primarily on CF_4 adsorption and capture. Of all porous materials that have been studied for CF_4 capture from N_2, only the isotypic metal–organic frameworks $Ni(ina)_2$ (ina^- = isonicotinate) and $Ni(3\text{-ain})_2$ (3-ain^{2-} = 3-aminoisonicotinate) display superior selectivities (Table S1†).[33] Importantly, however, they do not display the favorable stability to moisture that is inherent to Zn(fba), a critical trait for industrially viable prospective adsorbents for this separation. Unlike hydrophobic Zn(fba), which adsorbs minimal water, $Ni(3\text{-ain})_2$ and $Ni(ina)_2$ display type V water isotherms at 298 K (Fig. S9†). The isotherm steps seen upon adsorption are commensurate with framework decomposition and the formation of discreet nickel aqua complexes as reported previously (Fig. S10 and S11†).[49,50] In contrast, Zn(fba) is synthesized hydrothermally in neat water and displays unlimited stability to moisture at ambient temperatures while also adsorbing minimal water vapor (Fig. S9†). Given the frequent use of wet scrubbing to remove caustic water-soluble components of etch gas exhaust,[10] the moisture stability of Zn(fba) could allow it to be implemented downstream of wet scrubbing for CF_4 capture.

Although large selectivities for CF_4 over N_2 are achievable, establishment of equilibrium during CF_4 sorption is quite sluggish. The use of long equilibration intervals (180 s) are necessary to obviate substantial hysteresis between adsorption and desorption sweeps of isotherm measurements. Given that the trifluoromethyl-lined channels (6.0 Å diameter) are significantly larger than CF_4 (kinetic diameter of 4.7 Å), the observation of slow uptake kinetics suggested that CF_4 might manage to access the constricted arene-lined channels. Structural studies were undertaken to address this possibility. The accessibility of large, rod-shaped crystals of Zn(fba) facilitates the structural characterization of adsorbate-loaded samples using single-crystal X-ray diffraction. Using a home-built setup

(Fig. S17†), a single crystal housed within a thin borosilicate capillary was heated *in vacuo* and then dosed with CF_4 (1 bar) at 298 K, flame-sealed, and placed onto a diffractometer goniometer head. Although precise atomic coordinates for adsorbed CF_4 could not be reliably modeled owing to rotational disorder and high site symmetry, analyses of residual density after modeling and refining all framework atoms allowed for a qualitative location of adsorbed CF_4 (Fig. 4). The crystallographic data strongly suggest the primary adsorption site for CF_4 to be the arene-lined pores, which show substantial amounts of positive residual density following CF_4 dosing, while crystallographic analysis of the activated material shows essentially no residual density at this site (Fig. S18†). In contrast, minimal residual density is seen in the larger cylindrical channels lined with –CF_3 groups.

After data collection at 298 K, the cryostat temperature was lowered to facilitate additional CF_4 adsorption. Lowering the temperature on this closed system results in additional positive density appearing in the arene-lined pores (Fig. 4). Accordingly, these data suggest that the constricted arene-lined pores serve as primary adsorption sites for CF_4 and are responsible for the large magnitude of $-\Delta H_{ads}$ and the sizeable selectivity for CF_4 over N_2. We note also that dosing a crystal of Zn(fba) with methane (1 bar) results in the appearance of positive residual density within the arene-lined pores (Fig. S19†), although the smaller number of electrons in one molecule of CH_4 compared to CF_4 complicates the analysis of methane adsorption sites.

Further substantiation for preferential adsorption within the arene-lined channels was obtained from solid-state magic-angle spinning ^{19}F NMR measurements of CF_4-dosed samples. Activated Zn(fba) gives rise to a broad peak centered at −64.5 ppm corresponding to the –CF_3 groups of the fba^{2-} linker (Fig. S14†). Samples dosed with CF_4 were rapidly transferred into a solid-state rotor and sealed for NMR measurements.[52] Adsorbed CF_4 gives rise primarily to a single sharp peak that, based on
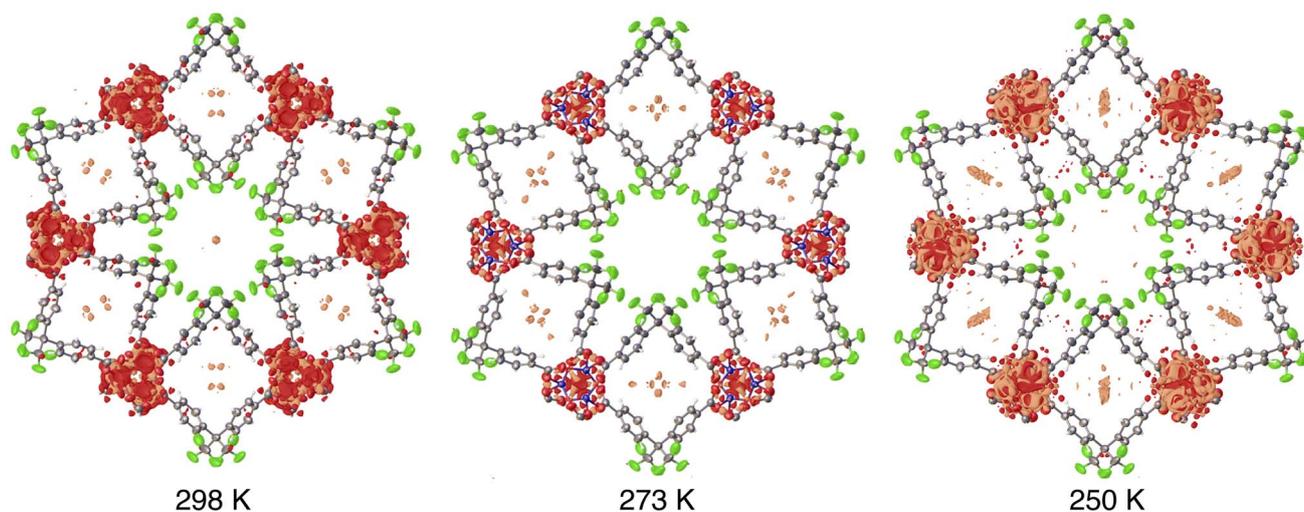
Fig. 4 Residual electron density within CF_4-dosed Zn(fba). A crystal of Zn(fba) housed within a borosilicate capillary was dosed with 1 bar CF_4 at ambient temperature, flame sealed, and mounted onto a diffractometer goniometer head. Data collection was performed at 298 K, 273 K, and 250 K. The capillary was allowed to equilibrate for at least 2 h at the analysis temperature prior to data collection. Orange and red regions correspond to positive and negative residual density, respectively. Electron density maps were generated using the Olex2 software package.[51] Isosurface values are set at 0.28 e Å^{-3}.

correlation with crystallographic measurements, we posit is attributable to CF_4 adsorbed within the arene-lined channels (Fig. 5 and S15†). A very small shoulder on the downfield side of this peak is also evident, which we suggest corresponds to a small quantity of CF_4 adsorbed within the cylindrical fluorinated channels. While the two peaks corresponding to adsorbed CF_4 occur at too similar of chemical shifts to deduce meaningful distinctions about the electronic environments at each adsorption site, these measurements buttress the

Fig. 5 Solid-state ^{19}F NMR spectra of CF_4-loaded Zn(fba) (grey trace) and spectral models of the signal corresponding to the linker $-CF_3$ groups (blue trace) and CF_4 adsorbed at the primary adsorption site (purple trace). To accurately model a shoulder on the downfield side of the data, a small second peak corresponding to a distinct CF_4 environment was included (red trace).

crystallographic observation of adsorption at primarily one chemically unique site at ambient temperature and pressure.

As frequently seen for metal–organic frameworks comprised of metal–oxide infinite chains, Zn(fba) is produced as rod-shaped crystals for which the long dimension corresponds to the crystallographic c axis (Fig. 6a). In the absence of defects,[53] substrate diffusion through a given channel should occur exclusively along the c axis. Scanning electron microscopy (SEM) images of as-synthesized Zn(fba) reveal a large dispersity of particle sizes that range from microcrystalline powders to large rod-shaped crystals. By pelletizing and sieving samples of Zn(fba), we were able to obtain bulk samples with a smaller size dispersity, owing primarily to the removal of the smallest fraction of microcrystallites (Fig. S31†). Although equilibrium CF_4 uptakes differ negligibly between sieved and non-sieved samples of Zn(fba) (Fig. S12†), transient adsorption experiments at 298 K reveal modestly quicker CF_4 uptake by non-sieved batches of material, consistent with the removal of the smallest particles from these samples (Fig. S21†). Interestingly, as shown in Fig. 6b, there is a large difference in the rates of adsorption between CF_4 and CHF_3, despite the fact that the effective sizes of these adsorbates should be rather similar. This observation demonstrates that the pore windows in Zn(fba) are appropriately sized to engender large differences in C_1 gas diffusivities as a function of adsorbate size.

Assuming uniaxial guest transport through a crystallite, diffusion can be treated as occurring through a plane sheet of length l. Provided that measurements are performed within the linear regime of the isotherm, the transient adsorption data can be modeled as described by Crank.[54] Adsorption of CF_4 within Zn(fba) is particularly well suited to kinetic analysis using transient adsorption data obtained on a sorption analyzer that uses the volumetric dosing method (in our case, a Micromeritics 3Flex). The sluggish nature of adsorption means that
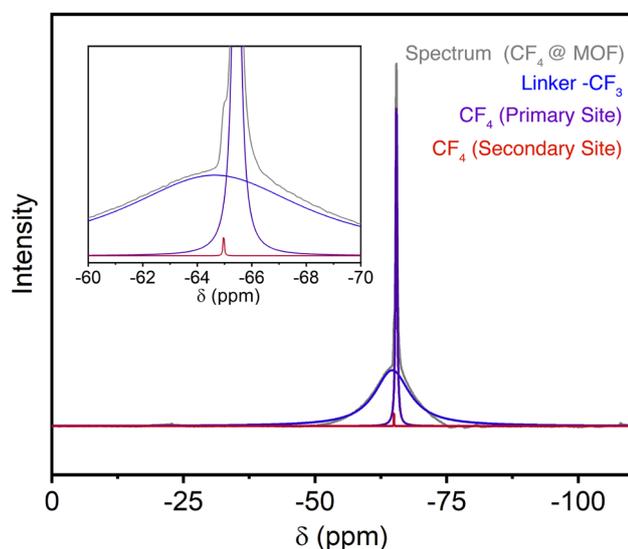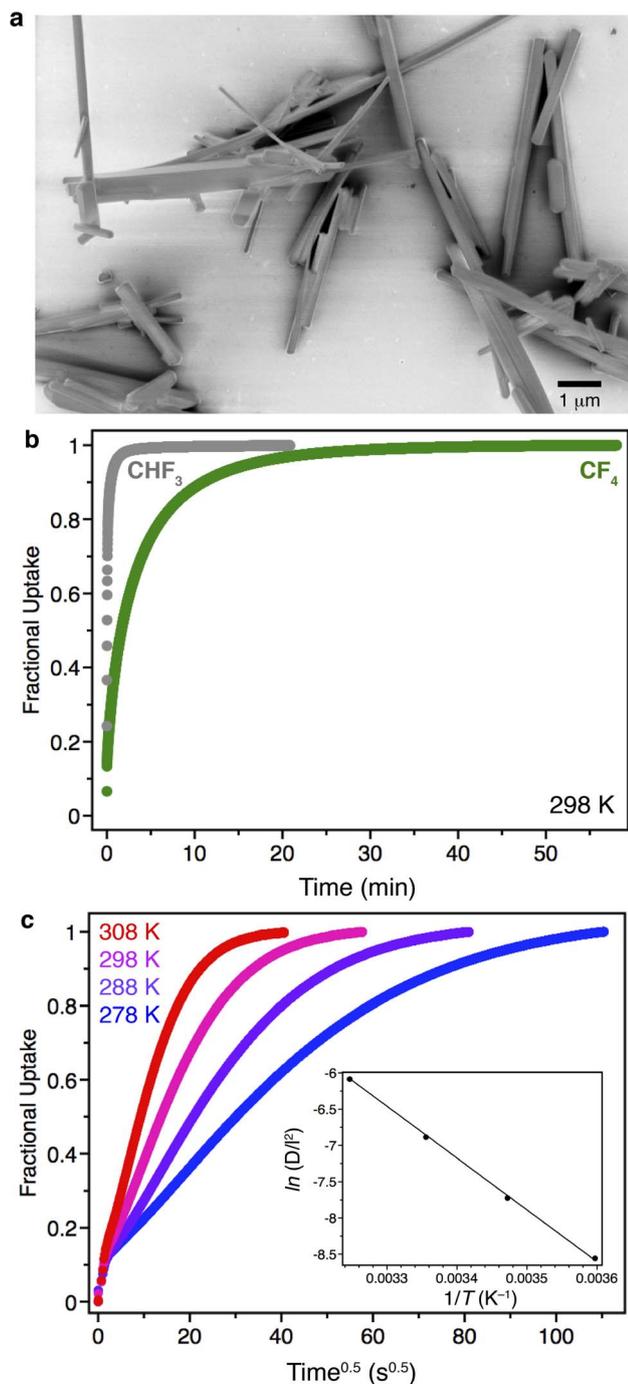
Fig. 6 (a) SEM image of sieved Zn(fba) showing a wide dispersity of crystallite sizes. (b) Transient adsorption data for CF_4 (green) or CHF_3 (grey) adsorption in Zn(fba) following a 1.00 mmol g^{-1} dose at 298 K. (c) Variable temperature CF_4 transient adsorption data from which values of D/l^2 were calculated. The inset shows the Arrhenius plot from which the activation energy of diffusion was determined.

only a small fraction of adsorption occurs within the first few seconds of a measurement, when valve opening and gas equilibration between the manifold and sample tube obfuscates the attribution of pressure changes to a given process. For CF_4 adsorption in Zn(fba), we can conveniently discard this portion

of the transient adsorption data, only modeling time points that correspond to a closed system free of gas-phase concentration gradients.

In our transient adsorption measurements, a sufficiently small dose of CF_4 (1.00 mmol g^{-1}) was used such that the equilibrium quantity adsorbed (0.12 mmol g^{-1} at 298 K) can be approximated to lie within the linear region of the isotherm (see Fig. 3a). After the first few seconds, a pronounced region of linearity is seen when fractional uptake (q_t/q_e) is plotted against square root time (Fig. 6c). The parameters q_t and q_e correspond here to the adsorbed quantities at time t and at equilibrium, respectively. If modeled assuming diffusion through a plane sheet, the slope in this region corresponds to (D/l^2), where D is the intracrystalline diffusivity for CF_4. Importantly, measurements using either different CF_4 dose quantities or different amounts of Zn(fba) result in minimal changes to the transient adsorption profile and the extracted D/l^2 quantity, indicating that bed transfer effects (*e.g.* interparticle diffusion) are negligible (Fig. S22 and S23†).[55] Additionally, we note that semilogarithmic plots of $1 - (q_t/q_e)$ *vs.* time display a slight positive curvature at earlier timepoints rather than being linear, which was pointed out by Snurr and Farha as being indicative of particle surface entry barriers to adsorption (Fig. S24†).[55] Accordingly, our transient adsorption data appear in excellent agreement with the notion that intraparticle diffusion represents the primary kinetic event controlling adsorption in Zn(fba). The large dispersion of Zn(fba) particle sizes obviates a determination of the size-independent intrinsic diffusivity, D. However, given that the particle length l is not a function of temperature, the temperature dependence of D/l^2 can be used to ascertain the effective activation barrier that corresponds to intraparticle CF_4 diffusion. Use of the Arrhenius model results in a diffusion barrier of 59(1) kJ mol^{-1} (Fig. 6c, inset).

Our crystallographic and kinetic insights into CF_4, CHF_3, and CH_4 adsorption suggest that single-file molecular diffusion through the corrugated arene-lined channels results in a sluggish adsorption profile for the larger-sized CF_4. This phenomenon is attributable to the constricted windows present along these channels, the dimensions of which will be dependent upon the orientations of the arene ring edges (Fig. 7).[56] Importantly, there is no significant difference in the crystallographic orientations of fba^{2-} linkers between the activated and CF_4-loaded structures of Zn(fba) (Fig. S20†). Successful access of these channels by CF_4 suggests a dynamic nature to the pore window, likely attributable to thermally activated aryl ring rotation, as the window width determined crystallographically (3.0 Å) is too small to permit access to CF_4. This situation evokes the adsorption kinetics profile of ZIF-8, whereby rotation of the 2-methylimidazolate linker controls the pore window dimensions and modulates adsorption kinetics of C_3 hydrocarbons.[57,58] We additionally note that Griffin and Dincă have measured the barrier to rotation within Zn_2(TCPE) (TCPE = tetrakis(4-carboxyphenyl)ethylene) to be 43(6) kJ mol^{-1}.[59] Like Zn(fba), this material contains 4-carboxyphenyl donors bearing a geminal relationship. While the exact barrier for ring rotation in Zn(fba) will be a function of both the local steric environment of an isolated fba^{2-} linker and the rigidity imposed by the MOF
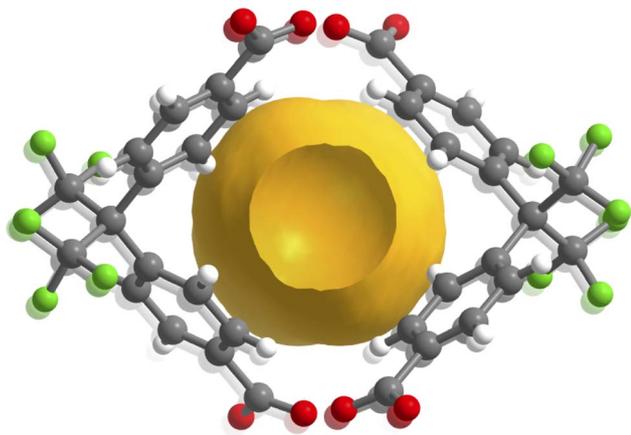
Fig. 7 Cross-sectional view down one of the arene-lined corrugated channels in Zn(fba). Two connected void regions are shown, depicting the accessible contact surfaces within the pore's largest region (background) and the window's narrowest point (foreground).

lattice, our structural analysis suggests that this value likely serves as a lower bound for the CF_4 diffusion barrier.

Multi-component ($5:95$ $CF_4:N_2$) breakthrough experiments were undertaken to assay the ability of Zn(fba) to separate this mixture under flowing mixed gas conditions. These experiments confirm successful resolution of these gases, albeit at relatively slow flow rates. When using an inlet flow rate of 3 sccm, CF_4 takes approximately 50% longer to break through a column packed with Zn(fba) compared to a column instead packed with an equivalent length of glass wool (Fig. S25 and S26†), while no change in total outlet flow rate is observed over the course of the experiments. However, the CF_4 breakthrough time becomes still longer when instead using a column packed with an activated charcoal (see the General considerations section of the ESI† for details) that has a similar CF_4 equilibrium capacity but exhibits a much smaller CF_4/N_2 IAST selectivity of 7.9 (Fig. S13†). Increasing the inlet flow rate to 20 sccm still allows for a modest amount of resolution between these gases by Zn(fba) as assayed by a longer CF_4 breakthrough time in comparison to a sorbent-free column (Fig. S27 and S28†). Owing to the hydrophobic nature of Zn(fba), the use of humid CF_4/N_2 streams results in no significant difference in the CF_4 breakthrough time (Fig. S29†). Accordingly, these experiments confirm that the corrugated ultramicropores within Zn(fba) can facilitate the separation of CF_4/N_2 mixtures, while simultaneously highlighting the need for faster diffusion kinetics to unlock the full potential of this material for applications in CF_4 capture.

Conclusions

The discovery of a very high equilibrium selectivity for CF_4 adsorption within Zn(fba) illustrates the potential of MOFs bearing hydrophobic ultramicropores to adsorptively capture PFC gases from industrial point emission sources. The stability of this material to moisture (and liquid water) is a critical trait that is shared by activated carbons and zeolites, although no examples from these classes of materials have shown CF_4

selectivities approaching that of Zn(fba). Strong CF_4 adsorption is a result of the close match in dimensions between the adsorbate molecules and the arene-lined pores. However, the large differences in the adsorption kinetics between CF_4 and CHF_3 highlights the challenges inherent to this design strategy – namely, that pore sizes approaching the dimensions of the adsorbate can lead to unfavorable kinetic profiles. While our study demonstrates the previously unappreciated accessibility of the arene-lined channels in Zn(fba) to small adsorbates, it also paints a picture of linker dynamics that are key to governing diffusion. Modulation of pore window character – an endeavor that is accessible using the principles of MOF pore engineering – should provide opportunities to alter adsorption kinetics while maintaining the favorable selectivities and physical properties embodied by the parent material. Synthetic endeavors in pursuit of this goal are currently underway in our laboratory.

Author contributions

Measurement and analysis of gas sorption (equilibrium and kinetic) data was performed by B. S. W., H. A. S., and B. R. B. Crystallographic data was collected and analyzed by B. S. W. and W. W. B. Scanning electron microscopy and thermogravimetric analysis data was collected and analyzed by B. S. W. Solid-state NMR data was collected and analyzed by J. K. and P. J. M. Column breakthrough data was collected and analyzed by S. S. M. and M. D. P. The manuscript was written by B. R. B., with all authors providing input and approving of the final submitted version.

Conflicts of interest

There are no conflicts to declare.

Acknowledgements

Notes and references

1 IPCC, *Climate Change 2023: Synthesis Report*, ed. Core Writing Team, H. Lee and J. Romero, IPCC, Geneva, Switzerland, 2023, DOI: **10.59327/IPCC/AR6-9789291691647**.

2 IPCC, *Global Warming of 1.5 °C*, ed. V. Masson-Delmotte, P. Zhai, *et al.*, 2018, http://www.ipcc.ch/report/sr15.

3 M. Bui, C. S. Adjiman, A. Bardow, E. J. Anthony, A. Boston, S. Brown, P. S. Fennell, S. Fuss, A. Galindo, L. A. Hackett, J. P. Hallett, H. J. Herzog, G. Jackson, J. Kemper, S. Krevor, G. C. Maitland, M. Matuszewski, I. S. Metcalfe, C. Petit, G. Puxty, J. Reimer, D. M. Reiner, E. S. Rubin, S. A. Scott, N. Shah, B. Smit, J. P. M. Trusler, P. Webley, J. Wilcox and N. MacDowell, *Energy Environ. Sci.*, 2018, **11**, 1062–1176.

4 R. L. Siegelman, E. J. Kim and J. R. Long, *Nat. Mater.*, 2021, **20**, 1060–1072.

5 H. M. Breunig, F. Rosner, T.-H. Lim and P. Peng, *Energy Environ. Sci.*, 2023, **16**, 1821–1837.

6 E. S. Sanz-Pérez, C. R. Murdock, S. A. Didas and C. W. Jones, *Chem. Rev.*, 2016, **116**, 11840–11876.

7 A. S. Bhown and B. C. Freeman, *Environ. Sci. Technol.*, 2011, **45**, 8624–8632.

8 S. Wang, S. Yan, X. Ma and J. Gong, *Energy Environ. Sci.*, 2011, **4**, 3805–3819.

9 *Environmental Protection Agency Overview of Greenhouse Gases*, https://www.epa.gov/ghgemissions/overview-greenhouse-gases, accessed December 2023.

10 M. B. Chang and J.-S. Chang, *Ind. Eng. Chem. Res.*, 2006, **45**, 4101–4109.

11 R. J. Cicerone, *Science*, 1979, **206**, 59–61.

12 B. K. Sovacool, S. Griffiths, J. Kim and M. Bazilian, *Renewable Sustainable Energy Rev.*, 2021, **141**, 110759.

13 B. A. Wofford, M. W. Jackson, C. Hartz and J. W. Bevan, *Environ. Sci. Technol.*, 1999, **33**, 1892–1897.

14 F. Iacopi and M. McIntosh, *Green Chem.*, 2019, **21**, 3250–3255.

15 F. Illuzzi, H. Thewissen and J. Integr, *Environ. Sci.*, 2010, **7**, 201–210.

16 J. Mühle, A. L. Ganesan, B. R. Miller, P. K. Salameh, C. M. Harth, B. R. Greally, M. Rigby, L. W. Porter, L. P. Steele, C. M. Trudinger, P. B. Krummel, S. O'Doherty, P. J. Fraser, P. G. Simmonds, R. G. Prinn and R. F. Weiss, *Atmos. Chem. Phys.*, 2010, **10**, 5145–5164.

17 J. M. Huck, L.-C. Lin, A. H. Berger, M. N. Shahrak, R. L. Martin, A. S. Bhown, M. Haranczyk, K. Reuter and B. Smit, *Energy Environ. Sci.*, 2014, **7**, 4132–4146.

18 Y. Zeng, R. Zou and Y. Zhao, *Adv. Mater.*, 2016, **28**, 2855–2873.

19 L. Zou, Y. Sun, S. Che, X. Yang, X. Wang, M. Bosch, Q. Wang, H. Li, M. Smith, S. Yuan, Z. Perry and H.-C. Zhou, *Adv. Mater.*, 2017, **29**, 1700229.

20 T.-H. Bae, M. R. Hudson, J. A. Mason, W. L. Queen, J. J. Dutton, K. Sumida, K. J. Micklash, S. S. Kaye, C. M. Brown and J. R. Long, *Energy Environ. Sci.*, 2013, **6**, 128–138.

21 D. Saha, Z. Bao, F. Jia and S. Deng, *Environ. Sci. Technol.*, 2010, **44**, 1820–1826.

22 Z. Niu, X. Cui, T. Pham, P. C. Lan, H. Xing, K. A. Forrest, L. Wojtas, B. Space and S. Ma, *Angew. Chem., Int. Ed.*, 2019, **58**, 10138–10141.

23 J. R. Li, R. J. Kuppler and H. C. Zhou, *Chem. Soc. Rev.*, 2009, **38**, 1477–1504.

24 S. Tsuzuki, T. Uchimaru, A. Wakisaka and T. Ono, *J. Phys. Chem. A*, 2016, **120**, 7020–7029.

25 A. Varadwaj, P. R. Varadwaj and B.-Y. Jin, *Int. J. Quantum Chem.*, 2015, **115**, 453–470.

26 J. Jagiełło, T. J. Bandosz, K. Putyera and J. A. Schwarz, *J. Chem. Soc., Faraday Trans.*, 1995, **91**, 2929–2933.

27 S. W. Choi, D.-H. Lee, J. Kim, J. Kim, J.-H. Park, H. T. Beum, D.-S. Lim and K. B. Lee, *Chem. Eng. J.*, 2017, **311**, 227–235.

28 X. Yuan, S. W. Choi, E. Jang and K. B. Lee, *Chem. Eng. J.*, 2018, **336**, 297–305.

29 S. W. Choi, H. J. Yoon, H. J. Lee, E.-S. Lee, D.-S. Lim and K. B. Lee, *Microporous Mesoporous Mater.*, 2020, **306**, 110373.

30 K. Tian, S. M. Elbert, X.-Y. Hu, T. Kirschbaum, W.-S. Zhang, F. Rominger, R. R. Schröder and M. Mastalerz, *Adv. Mater.*, 2022, **34**, 2202290.

31 I. Senkovska, E. Barea, J. A. R. Navarro and S. Kaskel, *Microporous Mesoporous Mater.*, 2012, **156**, 115–120.

32 T. H. Chen, I. Popov, W. Kaveevivitchai, Y. C. Chuang, Y. S. Chen, A. J. Jacobson and O. Miljanic, *Angew. Chem., Int. Ed.*, 2015, **54**, 13902–13906.

33 S.-M. Wang, H.-L. Lan, G.-W. Guan and Q.-Y. Yang, *ACS Appl. Mater. Interfaces*, 2022, **14**, 40072–40081.

34 Y. Wu, T. Yan, W. Zhang, S. Chen, Y. Fu, Z. Zhang and H. Ma, *Ind. Eng. Chem. Res.*, 2022, **61**, 13603–13611.

35 Z. Wan, T. Yan, M. Chang, M. Yang and D. Liu, *Sep. Purif. Technol.*, 2023, **306**, 122617.

36 J. Zhu, J. Hu, H. Xiao, L. Yang, M. Yang, S. Wang, J. Zhang and H. Xing, *Sep. Purif. Technol.*, 2024, **331**, 125614.

37 A. D. Yancey, S. J. Terian, B. J. Shaw, T. M. Bish, D. R. Corbin and M. B. Shiflett, *Microporous Mesoporous Mater.*, 2022, **331**, 111654.

38 K. P. Rao, M. Higuchi, K. Sumida, S. Furukawa, J. Duan and S. Kitagawa, *Angew. Chem., Int. Ed.*, 2014, **53**, 8225–8230.

39 S. Mukherjee, A. M. Kansara, D. Saha, R. Gonnade, D. Mullangi, B. Manna, A. V Desai, S. H. Thorat, P. S. Singh, A. Mukherjee and S. K. Ghosh, *Chem.–Eur. J.*, 2016, **22**, 10937–10943.

40 L.-H. Xie, M.-M. Xu, X.-M. Liu, M.-J. Zhao and J.-R. Li, *Adv. Sci.*, 2020, **7**, 1901758.

41 S. Mukherjee, K. K. R. Datta and R. A. Fischer, *Trends Chem.*, 2021, **3**, 911–925.

42 A. Monge, N. Snejko, E. Gutiérrez-Puebla, M. Medina, C. Cascales, C. Ruiz-Valero, M. Iglesias and B. Gómez-Lor, *Chem. Commun.*, 2005, 1291–1293.

43 J. Xie, F. Sun, C. Wang and Q. Pan, *Materials*, 2016, **9**, 327.

44 L. Yang, L. Yan, W. Niu, Y. Feng, Q. Fu, S. Zhang, Y. Zhang, L. Li, X. Gu, P. Dai, D. Liu, Q. Zheng and X. Zhao, *Angew. Chem., Int. Ed.*, 2022, **61**, e202204046.

45 T. Islamoglu, K. B. Idrees, F. A. Son, Z. Chen, S.-J. Lee, P. Li and O. K. Farha, *J. Mater. Chem. A*, 2022, **10**, 157–173.

46 C. M. Lastoskie, in *Characterisation of Porous Solids V*, ed. K. K. Unger, G. Kreysa and J. P. Baselt, Elsevier, 2000, vol. 128, pp. 475–484.

47 K. S. Walton and R. Q. Snurr, *J. Am. Chem. Soc.*, 2007, **129**, 8552–8556.

48 A. L. Myers and J. M. Prausnitz, *AIChE J.*, 1965, **11**, 121–127.

49 N. Gantzler, M.-B. Kim, A. Robinson, M. W. Terban, S. Ghose, R. E. Dinnebier, A. H. York, D. Tiana, C. M. Simon and P. K. Thallapally, *Cell Rep. Phys. Sci.*, 2022, **3**, 101025.

50 O. Pajuelo-Corral, I. J. Vitorica-Yrezabal, A. Rodríguez-Diéguez, J. M. Seco and J. Cepeda, *Inorg. Chem. Commun.*, 2024, **160**, 111872.

51 O. V Dolomanov, L. J. Bourhis, R. J. Gildea, J. A. K. Howard and H. Puschmann, *J. Appl. Crystallogr.*, 2009, **42**, 339–341.

52 Note that thermogravimetric analysis of CF_4-dosed Zn(fba) shows significant offgassing at low temperatures, demonstrating that CF_4-loaded MOF can be briefly manipulated in the absence of CF_4 without undergoing thorough loss of adsorbate. See Fig. S16 in the ESI†.

53 A. C. Forse, M. I. Gonzalez, R. L. Siegelman, V. J. Witherspoon, S. Jawahery, R. Mercado, P. J. Milner, J. D. Martell, B. Smit, B. Blümich, J. R. Long and J. A. Reimer, *J. Am. Chem. Soc.*, 2018, **140**, 1663–1673.

54 J. Crank, *The Mathematics of Diffusion*, Clarendon Press, Oxford, 2nd edn, 1975.

55 F. A. Son, B. C. Bukowski, T. Islamoglu, R. Q. Snurr and O. K. Farha, *Chem. Mater.*, 2021, **33**, 9093–9100.

56 C. H. Sharp, B. C. Bukowski, H. Li, E. M. Johnson, S. Ilic, A. J. Morris, D. Gersappe, R. Q. Snurr and J. R. Morris, *Chem. Soc. Rev.*, 2021, **50**, 11530–11558.

57 K. Li, D. H. Olson, J. Seidel, T. J. Emge, H. Gong, H. Zeng and J. Li, *J. Am. Chem. Soc.*, 2009, **131**, 10368–10369.

58 B. R. Barnett, M. I. Gonzalez and J. R. Long, *Trends Chem.*, 2019, **1**, 159–171.

59 N. B. Shustova, T.-C. Ong, A. F. Cozzolino, V. K. Michaelis, R. G. Griffin and M. Dincă, *J. Am. Chem. Soc.*, 2012, **134**, 15061–15070.